ELSEVIER

Contents lists available at ScienceDirect

Surfaces and Interfaces

journal homepage: www.sciencedirect.com/journal/surfaces-and-interfaces



Enhanced piezoelectric performance of multilayered piezoelectric nanogenerator based on the PVDF/PZT/graphene Electrospun for IoT-based remote monitoring

Ertuğrul Karakulak ^a, Levent Paralı ^{b,*}, Muhterem Koç ^c, Farida Tatardar ^d, Ali Sarı ^e, Ersoy Mevsim ^a, Valida Fataliyeva ^d

- ^a Tekirdağ Namık Kemal University, Vocational School of Technical Sciences, Tekirdağ, 59860-Turkey
- ^b Manisa Celal Bayar University, Department of Electronics and Automation, Manisa, 45400-Turkey
- ^c Kütahya Dumlupınar University, Department of Industrial Design, Kütahya, 43100-Turkey
- ^d Khazar University, Mahsati str. 41, AZ 1096, Baku, Azerbaijan
- ^e Manisa Celal Bayar University, Department of Electrical and Energy, Turgutlu, Manisa 45400-Turkey

ARTICLE INFO

Keywords: PVDF PZT Graphene Electrospinning Multilayered electrospun Internet of things-IoT

ABSTRACT

This research focused on improving the performance of piezoelectric nanogenerators by utilizing a piezoelectric nanogenerator (PNG) design that combines stacked piezoelectric electrospun nanofibers with conductive layers placed between them. A polyvinylidene fluoride (PVDF)/lead zirconate titanate (PZT)/unmodified graphene nanoplatelet (GNP) based multilayered structure (MLS) was produced as a parallel connection using a layer-by-layer assembly technique. At a vibrational frequency of 20 Hz, under a resistance load of 50 k Ω , the four-layered PNG reached an open-circuit voltage of 0.18 V(V_{RMS}), a maximum electrical power of 0.166 μ W (P_{RMS}) by drawing a current of 1.82 μ A (I_{RMS}). The four-layered PNG, which exhibits high capacitance and low impedance characteristics, has increased the full charging voltage (3.96 V) to 80% compared to a single-layered PNG (2.2 V). Furthermore, the electrical power obtained from the four-layered PNG was approximately 4.38 times higher than the single-layered one. The resulting multilayered PNG (M-PNG) can be utilized effectively in self-powered wireless e-health systems for detecting human movement.

1. Introduction

With the increase in smart electronic devices based on the Internet of Things (IoT), the need for sustainable, renewable, and distributed energy sources for advanced sensor networks is growing by the day. Batteries are still preferred as a power supply for electronic devices despite their limited lifetime, periodic maintenance requirements, and pollution drawbacks, such as environmental waste [1]. Therefore, there has been a significant increase in research on sustainable technologies for generating energy from renewable sources such as mechanical, wind, solar, and thermal. In particular, nanogenerators that convert mechanical energy from the environment into electricity via various mechanisms have been the focus of attention. These mechanisms include piezoelectric [2], triboelectric [3], electromagnetic [4], and pyroelectric effects [5]. Among them, piezoelectric material and energy harvesters offer promising alternatives owing to their simple, flexible, and

high-power density properties for use as a sustainable power supply for large sensor networks in IoT applications [6].

Smart building technology consists of various components that work together seamlessly, such as sensors, IoT devices, automation systems, and communication protocols. With the rapid development of artificial intelligence (AI) and IoT technologies, wearable electronics-based devices have begun to attract significant interest. Especially with the advent of the IoT era, the demand for systems containing numerous sensor nodes in various application areas is steadily increasing [7]. Wireless, sustainable, and autonomous operation requirements are becoming increasingly important for large-scale sensor networks and systems. For these purposes, self-powered sensing systems that can utilize energy harvested from their surroundings to directly detect external stimuli have garnered significant interest. The invention and rapid development of nanogenerators, which utilize Maxwell's displacement current as a driving force, have spurred research into self-powered

E-mail address: levent.parali@cbu.edu.tr (L. Paralı).

 $^{^{\}ast}$ Corresponding author.

active mechanical sensors, electronic coatings, and human-robot interaction [8,9]. According to data from the International Data Corporation (IDC), the global IoT solutions market, which includes smart systems, connectivity services, infrastructure, applications, security, analytics and professional services, is reported to have achieved a compound annual growth rate of 20 %. Significant cash flow is expected in the IoT-based projects market globally between 2020–2030 [10].

Although inorganic materials such as barium titanate (BaTiO₃) and lead zirconate titanate (PZT) have relatively high piezoelectricity (piezo sensitivity and piezo modules), an dielectric constant, mechanical properties (strength, mechanical quality coefficient, and Young's modulus), an electromechanical boundary coefficient and a low loss tangent, their flexibility as applications are limited due to their low fracture stress, and fragile structures [11,12]. Therefore, they require different production methods, which include combining them with flexible polymer nanofiber materials. Recently, there have been reports of fabricating various composites, such as 0-3, 1-3, and 2-2 types by combining piezoelectric ceramics with polymers. These composites not only exhibit excellent flexibility but also achieve higher piezoelectric coefficient-d₃₃ and piezoelectric voltage constant-g₃₃ values, which are critical components of energy harvesting applications [13]. Since the mass production of composites with 0-3 types of connectivity is comparatively easy when compared to composites of other types, 0-3 type-based polymer-ceramic composites are widely preferred [14]. Furthermore, these materials combine the electrical properties of ceramics with polymers' flexibility and chemical stability. In recent years, electroactive polymers such as polyvinylidene difluoride (PVDF) and its copolymers (PVDF-TrFE: Polyvinylidene fluoride-trifluoro ethylene and PVDF-HFP: Polyvinylidene fluoride-hexafluoropropylene) have gained importance attributed to their high flexibility, electromechanical properties, voltage sensitivity, lightness, high chemical resistance, good biocompatibility, and low dielectric constant [15]. In particular, the PVDF has five crystal phases such as α (TGTG'), β (TTTT), γ (T3GT3G'), δ (TGTG') and ε (T3GT3G'), depending on their chain formations. Among these, the β phase with polar, which has the highest polarization and the most favorable ferroelectric properties, contributes to applications such as sensors, actuators, energy harvesting systems, filters, and polymer-based multiferroic composites[16].

Compared to other devices that perform electromechanical conversion, piezoelectric composites have higher electromechanical efficiency and exceptional scalability, allowing them to be miniaturized to the microelectromechanical systems (MEMS) scale [17,18]. For this reason, they are widely used in precision sensing and actuation applications [19]. However, as a result of intensive research on PVDF/PZT composites in the literature, 0-3 type composites still have not yet achieved high piezoelectric properties compared to sintered piezoelectric ceramics because of material bonding deficiencies caused by the random dispersion of ceramic particles in the polymer matrix [20,21]. Therefore, in order to strengthen the coupling between randomly dispersed ceramic particles in a polymer matrix, to enhance the β-phase of the PVDF, ternary composite structures resulting from incorporation of some third conductive phases, such as graphene [22], hydrated ionic salts [23], carbon nanotubes (CNTs) [24], and halides [25] into the polymer matrix have been the focus of attention. Although graphene, which has strong mechanical strength, excellent electrical conductivity, and thermal conductivity properties, does not have piezoelectric properties, it is known that the piezoelectric properties of PVDF/graphene composites are enhanced compared to those of pure PVDF. This demonstrates that the addition of graphene positively affects the crystalline phase of the PVDF [26,27]. Furthermore, considering recent studies on ternary composites with graphene content, it has been observed that graphene significantly improves both the beta phase fraction and the piezoelectric output effects compared to those composites without graphene [28–30]. On the other hand, when blending graphene directly into the polymer matrix via electrospinning, which is the simplest and most effective method, this process results in the graphene's electrical conductivity

being reduced as a result of its presence in an insulating polymer. However, in ternary composites, weak bonding between the different components causes a significant decrease in mechanical properties, such as tensile strength, flexural strength, and impact strength. It also causes deterioration in hardness and durability. The absence of strong interfaces means the material cannot withstand loads, resulting in early crack propagation and failure. This weakness can also create a negative impact on the composite material's thermal resistance, water absorption, the overall performance, and longevity of the composite material [31].

Furthermore, the low conductivity of the single-layered electrospun fibers, which are produced using the electrospinning method, causes residual charges to accumulate on their surfaces. Additionally, a decreased adhesion between fibers leads to a loose structure that exhibits a low-density and low-flexibility fiber network. This weak adhesion may be a result of insufficient polymer winding, high solution viscosity, or improper fiber alignment, resulting in a poor mechanical structure form. These negative factors reduce the output voltage performance of single-layered electrospun-based PNGs [32–34].

Thus, in order to improve the mechanical properties and the sensing applications by effectively combining electrospun nanofibers with graphene, various methods such as surface graft polymerization, physical adsorption-coating, layer-by-layer fabrication, chemical doping, plasma modification, heteroatom doping, and wet chemistry are widely used [35]. One of these methods, the layer-by-layer (LBL) fabrication process, involves vertically overlapping single-layer fiber mat structures to create multilayered structures (MLS) that can fit into the space available for the single-layer fiber. Recently, in order to achieve a high-performance piezoelectric nanogenerator (PNG), researchers have focused on the multilayered PNG (M-PNG), which is packed according to the dipole moment direction of electrospun fiber mats [36,37]. It has been shown that MLS with parallel connections exists in various LBL fabrications that have been shown to have higher piezoelectric properties than those that are built in a series [38]. Although some studies have been carried out on graphene-based MLS, there appears to be a lack of studies in the literature on multilayered piezoelectric ternary composite structures that utilize 0–3 type layering containing unmodified graphene nanoplatelets.

In this study, the flexible electrospun mats based on the pure PVDF and the PVDF/PZT/GNP were first produced by electrospinning. In order to determine the structural and morphological characteristics of the mentioned specimens, XRD: X-ray diffraction, FTIR: Fourier transform infrared, and SEM: scanning electron microscopy analyses were carried out, respectively. Thereafter, the PVDF/PZT/1.5 wt. %GNP-based PNG was fabricated by placing single and MLS (two, four, and six-layered with parallel connections) composites between conductive electrodes. Finally, the piezoelectric performances, such as voltage, current, and the maximum transfer values of the single-layered and M-PNGs placed on the piezoelectric energy harvesting system (PEHS), were examined. Furthermore, the design of a simple IoT-based wireless monitoring system to track the electrical signals captured from the M-PNGs fabricated in this study is also documented.

2. Materials and methods

2.1. Materials

PVDF powder (Molecular Weight: ~534.000 g/mol) was purchased as the host material from Sigma Aldrich, while a PZT-5A (APC 850/Navy Type II, APC International, Inc.) commercial powder and graphene nanoplatelets (Nova Scientific Resources-M Sdn. Bhd.) were selected as filler materials. Acetone and N-dimethylformamide-DMF (Merck-99.5%) were chosen for their ability to disperse and dissolve the materials. The typical characteristics of the PZT-5A powder (particle size of $<1~\mu m$) and unmodified graphene nanoplatelet (GNP) are shown in Tables 1 and 2, respectively.

Table 1The piezoelectric features associated with PZT-5A.

Piezoelectric Properties	PZT-5A / APC 850 / Navy Type II
Relative permittivity-εr (dielectric constant)	1900
Electromechanical coupling coefficient (k_{15} , k_{31} , k_{33})	0.68, 0.36, 0.72
Piezoelectric charge constants (d ₁₅ , d ₃₁ , d ₃₃)	590, 175, 400
Piezoelectric voltage constants (g ₁₅ , g ₃₁ , g ₃₃)	36, 12.4, 24.8
Young's modulus (-Y ^E ₁₁ , Y ^E ₃₃)	6.3, 5.4
Quality factor (Mechanical-Q _m)	80

Table 2Graphene Nanoplatelets properties.

Purity	99.5 %
Thickness	less than 32 layers, 4-20 nm
pH (Solution)	7 – 7.7 (30 °C)
Resistivity of volume	4×10^{-4} ohm. cm
Average diameter	5–10 μm
Analysis certificate	C=99.7 %, O <0.3 %

2.2. Methods

2.2.1. Fabrication of the single layered PNG based on the PVDF/PZT/GNP The fabrication stages related to pure PVDF and PVDF/PZT/1.5 wt. %GNP electrospun based PNGs are demonstrated in detail in Fig. 1. The initial solution was formulated by dissolving the PVDF powder (10 % w/ v) in a mixture of acetone and DMF (7:3) at a temperature of 80 $^{\circ}\text{C}$ for a duration of 2 hours, employing a magnetic stirrer to facilitate the process. Subsequently, the second solution was obtained by combining the PVDF solution with the commercial PZT-5A ceramic powder (15 vol. %) and the GNP in a weight ratio of 1.5 wt. % (Fig. 1(a)). The electrospun samples were produced using an electrospinning system that consists of a rotating drum collector, a syringe pump, a plastic syringe with a metal needle, and a direct current (DC) voltage source (Fig. 1(b)). In the production of electrospun mats, the aluminum foil-covered rotating drum collector was 2400 rpm. The pump used in the system delivered the solution at a rate of 4.0 ml/h, while the distance between the needle tip and the collector and the applied voltage were 15 cm and 17 kV, respectively. The two electrospun specimens previously referenced were examined to ascertain their structural and morphological characteristics. This examination involved a variety of analytical methods, including XRD, FTIR, and SEM.

During electrospinning, stretching and polarizing the β -PVDF molecular chains creates a dipole moment perpendicular to the β -phase PVDF crystal molecular chain direction, attributed to the difference in electronegativity between hydrogen (H) and fluorine (F). The fluorine (F) atom, which is the most electronegative, is oriented towards the positive electrode, while the hydrogen (H) atom, which is the least electronegative, is attracted to the negative electrode. (Fig. 1(c)). Consequently, the electrospinning process facilitates not only the β -phase formation of the PVDF but also enables the generation of a dipole moment at right angles (90 degrees) within the polymer chain structure [39]. Subsequently, the single-layered PNG device was constructed by positioning the electrospun mat, which measured 4 cm by 4 cm, between two conductive aluminum electrodes. As illustrated in Fig. 1(d), the electrical symbol of the single-layered PNG is represented by a color scheme that corresponds to the dipole moment direction.

2.3. Characterization

The phase compositions of the pristine PVDF and the PVDF/PZT/1.5 wt. % GNP electrospun samples were ascertained via phase analysis, which was conducted on X-ray diffractograms recorded at ambient temperature. The XRD diffractometer that was employed was a

PANalytical Empyrean, equipped with CuK radiation (1.5418 Å), and the SEM images of the samples were examined via SEM device (SUPRA 40VP). The FTIR spectra of the specimens, ranging from 1600 to 400 cm 1 , were examined using the Bruker FTIR-ATR system at room temperature. The capacitance, impedance, and dielectric properties were measured using an LCR meter (HIOKI-IM3536). It should be noted that these properties vary depending on frequency; therefore, the meter was utilized to obtain the samples' data at various frequencies. The piezoelectric performances ($V_{\rm OC}$ -the open circuit voltage, $I_{\rm SC}$ -the short circuit current, and the maximum power transfer capacities) of the PNGs were determined by PEHS, which has been specially selected. Under the impact force of 1 N, the open circuit voltages ($V_{\rm PP}$: peak-to-peak) related to the PNG were determined through a data logger (NI-6009), whereas a low noise current amplifier (LMC-6001) was used to measure their short circuit currents.

3. Results and discussion

3.1. Structural and morphological analysis

The XRD patterns of the pure PVDF and the PVDF/PZT/1.5 wt. % GNP fiber mats are depicted in Fig. 2. The diffraction peak at 20 at 20.17° [40] was attributed to the β -phase fraction of the pristine PVDF electrospun mat, while its α -phase fraction was defined as 2θ =18.14° [41]. The results of this study demonstrated the efficacy of the electrospinning process in converting the α -phase that was present in the PVDF chain structure into the electroactive β -phase. The composite electron-spun mat, based on the PVDF/PZT/1.5 wt. % GNP, exhibited the characteristic diffraction peaks of 22.32°, 31.99°, 38.28°, 44.23°, 50.18° , 55.26° , and 65° It has been determined that 17° planes are consistent with the crystalline perovskite phase of the PZT [42]. The diffraction peak observed at $2\theta = 26.20^{\circ}$ has been shown to correspond with the (002) plane of the GNP (JCPDS #98-003-1170). The integration of GNPs into the PVDF/PZT electrospun composite, as evidenced by the presence of GNPs within the composite, signifies the effective incorporation of GNPs into the PVDF/PZT composite [43].

Additionally, as demonstrated in Fig. 2, the degrees of crystallinity in the pristine PVDF and the PVDF/PZT/1.5 wt. %GNP samples have been delineated based on an analysis of the XRD pattern. The degree of crystallinity (χ c) can be evaluated according to Eq. (1) [44].

$$\chi_{C}(\%) = \frac{A_{C}}{A_{C} + A_{B}} \times 100$$
 (1)

where A_a is the area under the peaks meaning the total amorphous region and A_c is the area under the peaks constituting the total crystalline region. According to the calculated results, the degree of crystallinity of the PVDF/PZT/1.5 wt. %GNP (χ_C : 61.86) was 1.8 times greater than that of the pure PVDF (χ_C :33.76).

An increase in crystallinity in the PVDF/PZT/1.5 wt. %GNP composite generally improves piezoelectric performance by creating more regular structures that can generate a stronger electrical signal under mechanical stress. Higher crystallinity allows for better alignment of the areas responsible for the piezoelectric effect, which leads to an increase in output performances (voltage, current, and power), and overall piezoelectric coefficients. This effect is observed in polymer and ceramic materials where processes such as thermal treatment, mechanical stretching, self-powered (polarization during electrospinning), or filler addition can enhance piezoelectric responses by promoting the formation of well-defined crystalline regions [45,46].

The FTIR results that were realized for the pure PVDF and the PVDF/PZT/1.5 wt. % GNP electrospun mats are indicated in Fig. 3. The β -phase ratio of all specimens was calculated by taking into consideration two different peaks and absorption wavenumbers of 840 cm⁻¹ and 762 cm⁻¹ using the Lambert-Beer law as stated by the following Eq. (2).

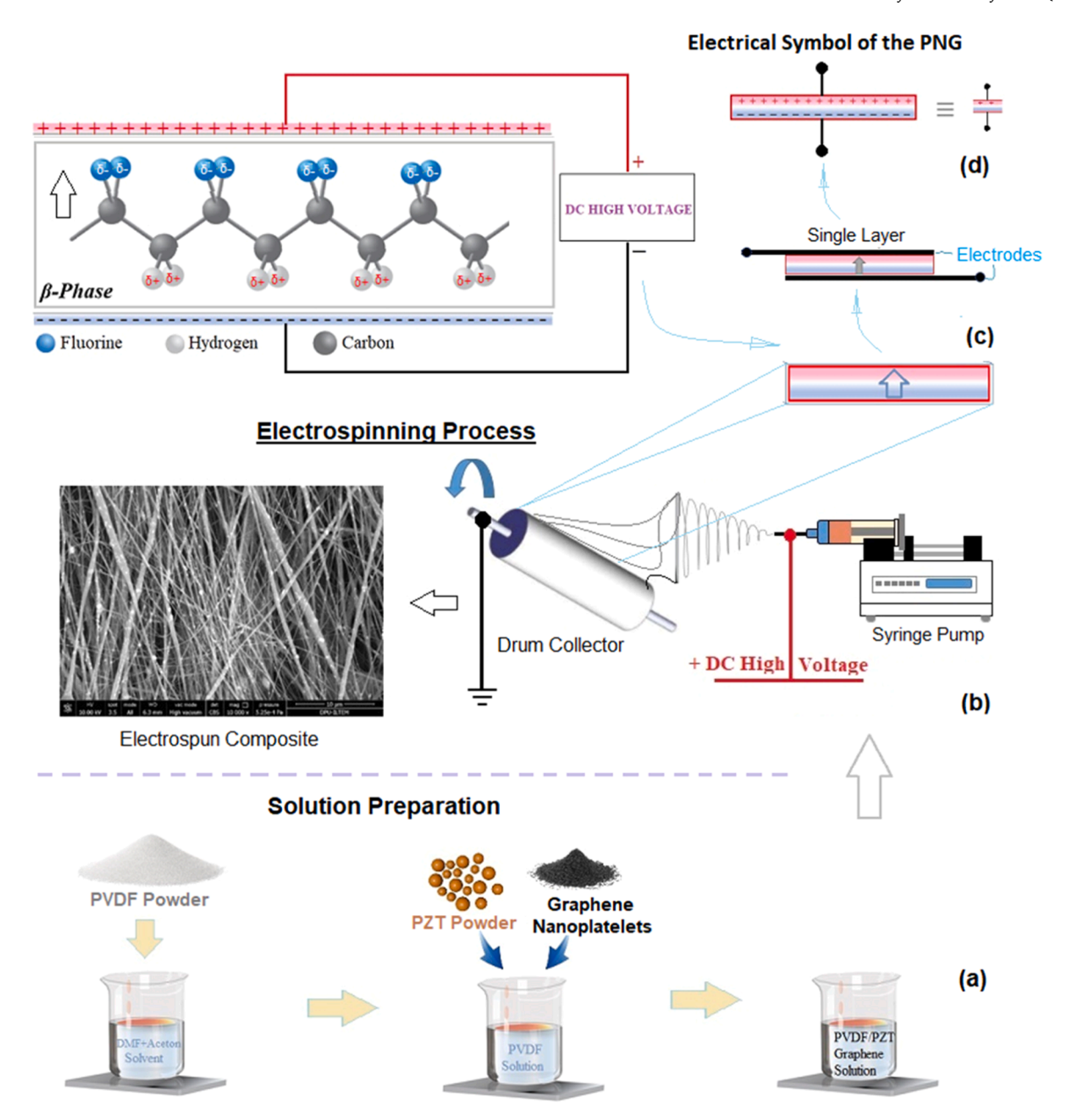


Fig. 1. The schematic demonstration of the PNG based on the pristine PVDF and the PVDF/PZT/1.5 wt. %GNP electrospun composite consist of: Solution preparation (a), electrospinning process (b), a dipole moment formation in the perpendicular direction along the polymer chain structure owing to stretching and the effects of high voltage direct current (DC), and the single layered PNG fabrication (d).

$$\%F(\beta) = \frac{A_{840}}{1.26A_{762} + A_{840}} x100 \tag{2}$$

where A_{840} and A_{762} are the absorbance values of the sample at the respective wavenumbers (840 cm⁻¹ and 762 cm⁻¹), and 1.26 is the value calculated from K_{840}/K_{762} (where K_{840} is the molar absorptivity at 840 cm⁻¹ = 7.7×10^4 cm²/mol, and K_{762} is the molar absorptivity at 762 cm⁻¹ = 6.1×10^4 cm²/mol) [47].

The peak analyzer software (Origin software version 2022-b-Learning Edition) was used to calculate the percentage of the β -phase contents of the samples. As depicted in Fig. 3, the β -phase content of the PVDF/PZT/15 wt. % GNP-based electrospun sample was the highest at 95.89 %, which was 1.36 times higher than that of the pure PVDF (70.44 %).

In addition, the elevated regions illustrated in Fig. 3 for the pure PVDF and the PVDF/PZT/1.5 wt. % GNP electrospun at the vibration bands of 482 [48], 502 [49], 836 [50], 876 [51], 1067 [52], 1170 [53],

1268 [54], and 1400 cm $^{-1}$ [55] are ascribed to the β -phase, whereas the peaks at 606 [56] and 756 cm $^{-1}$ [57] are as a result of the α -phase for all specimens. As the amount of crystalline formations in the samples increased, α -phase formations decreased rapidly, as shown by the FTIR results. The electrospinning process involves stretching the fibers mechanically through a rotating collector. This stretching promotes the formation of crystal arrays on the electrospun fibers, resulting in a higher content of the β -phase [58].

Fig. 4 depicts the SEM images of the pristine PVDF electrospun fiber and PVDF/PZT/1.5 wt. % GNP electrospun composite. Although the surface of the pure PVDF fiber (Fig. (4a)) is smooth as a result of the absence of fiber adhesion and non-volatile solvents, the addition of the PZT ceramics (Fig. (4b)) creates a pattern of mosaic on the composite fibers' surfaces. Fig. 4b shows a homogeneous dispersion of PZT in a regularly oriented polymer matrix. Moreover, the presence of GNP-based conductive structures in the solution increased the Coulombic forces and the electrostatic repulsion during the electrospinning process,

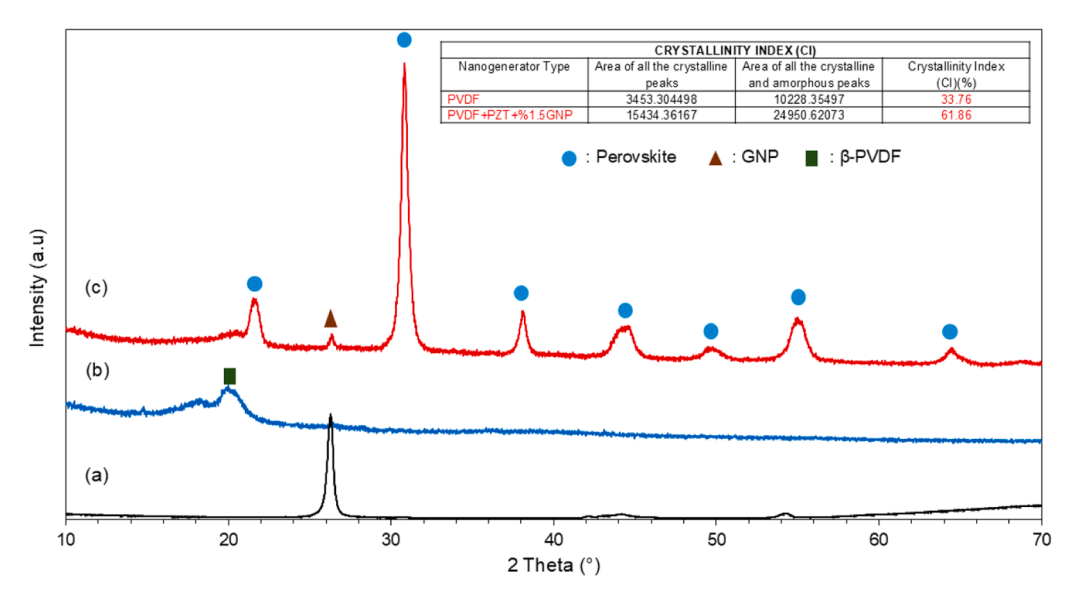


Fig. 2. The XRD diffractograms of the GNP powders (a), the pure PVDF (b) and the PVDF/PZT/1.5 wt. %GNP electrospun mats (c).

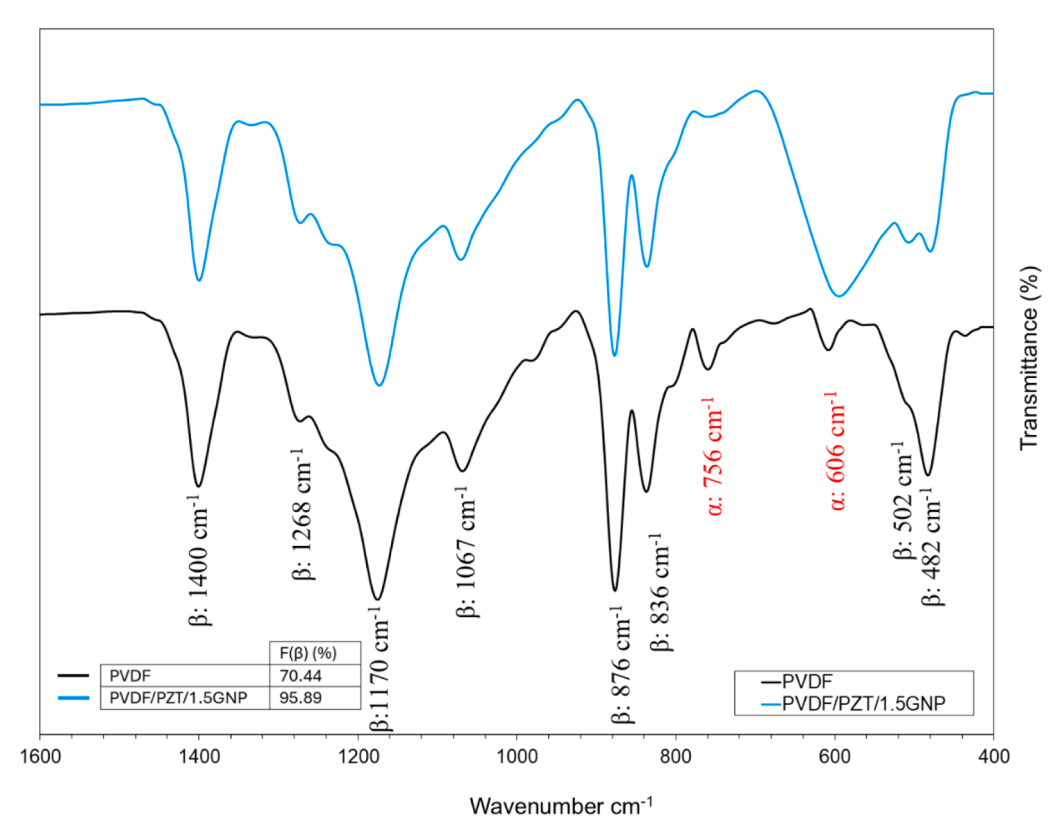


Fig. 3. FTIR spectrum of the pristine PVDF and fiber composite based on the PVDF/PZT/1.5 wt. %GNP.

leading to a progressive irregularity of the fiber thickness in the composite structure [59].

3.2. LBL assembly of the M-PNGs

Single-layered electrospun mats have weak and unstable output signals attributed to their loose structures. To improve the electromechanical performance of composite structures, recent studies have focused on multilayer architectures [36,60]. Fig. 5 provides a comprehensive overview of the M-PNG fabrication process.

As seen in Fig. 5, aluminum sheets were used not only for the bottom

and top electrodes, but also between the stacked electrospun mat layers, in order to promote electron flow when joining the layers. The electrospun mats were assembled in designs of 2, 4, and 6 layers and were pressed using the pressing process at 15 MPa for 60 min at room temperature (Fig. 5a, b). The copper wires were bonded to the electrode tips with silver adhesive after all the specimens were pressed. The sandwich structure was fully preserved by wrapping it with thin Kapton tape. The structure was covered with a PVC film (thickness: $25~\mu m$) at a temperature of $120~^{\circ} C$ to create a more uniform packaging structure. As shown in Fig. 6, the single-layered and parallel-type composites were obtained by combining electrospun composites according to their dipole moment

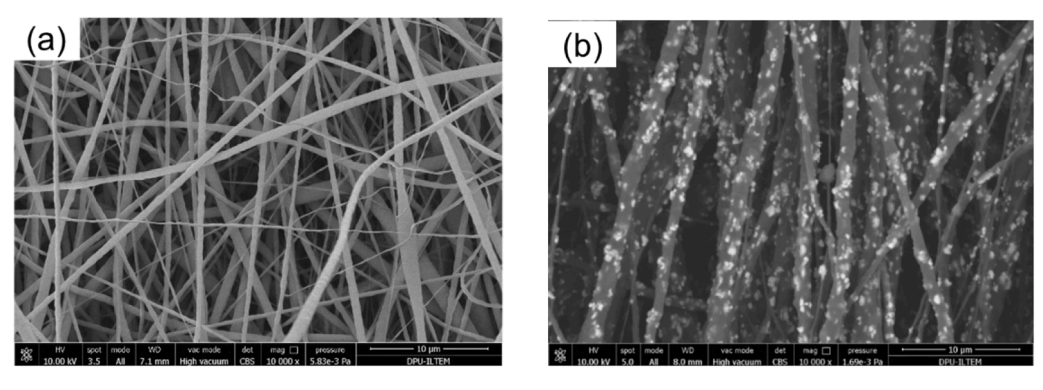


Fig. 4. SEM images of the pristine PVDF (a) and the PVDF/PZT/1.5 wt. %GNP (b) electrospun mats.

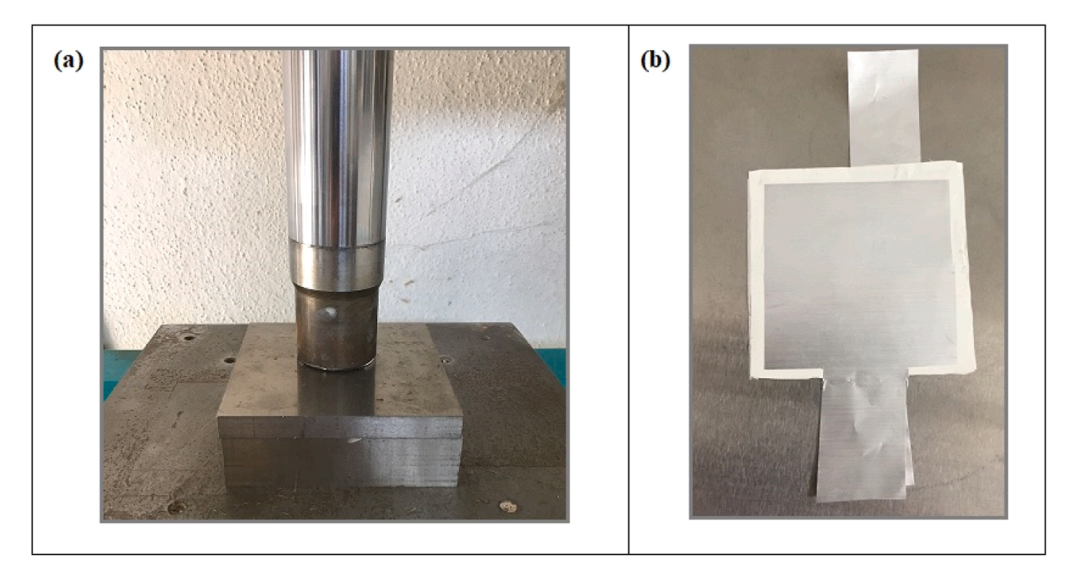


Fig. 5. The M-PNG encompasses the manufacturing architecture, the pressing process (a), and the photographing of the fiber mats after the processing step (b).

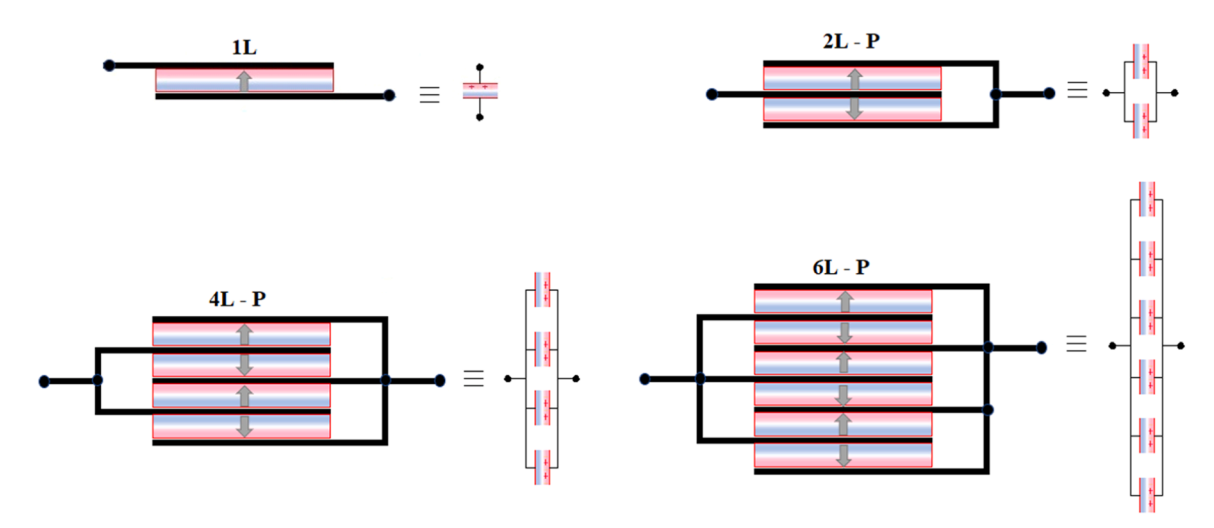


Fig. 6. Schematic designs of the single and M-PNGs (two: 2L-P, four: 4L-P, and six-layered: 6L-P) with a parallel type and their electrical equivalent circuits.

directions.

As shown in Fig. 7, the surface image of the four-layered PVDF/PZT/ 1.5 wt. % GNP composite reveals that the fibers on the composite's surface have been compressed and the fiber density has been increased. The composite structure formed with the aluminum electrode placed between two fiber mats was pressed together and had an average

thickness of 80 $\mu\text{m}.$

3.3. Dielectric properties of PNGs

Fig. 8 presents the single and M-PNGs' dielectric characteristics, respectively. The ϵ_r values of the PNG as a function of frequencies from 1

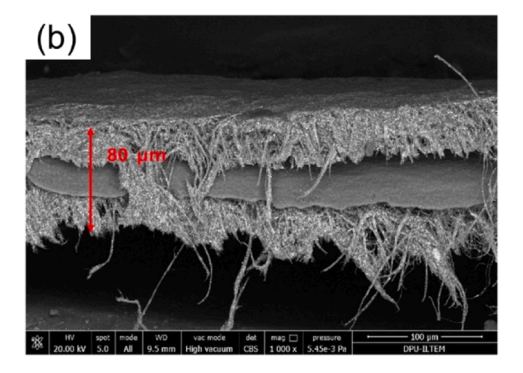
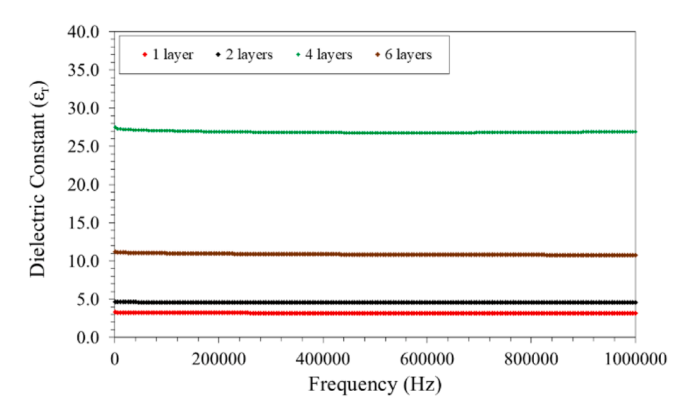


Fig. 7. SEM images of the surface fibers of the single-layered PNG (a) and a cross-section of MLS (b).



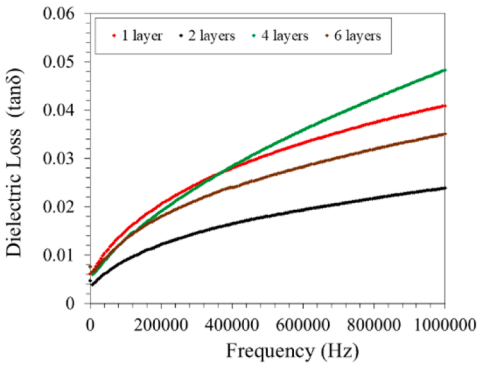


Fig. 8. Dielectric constant-εr (a) and dielectric loss-tanδ (b) changes at frequencies from 1 kHz to 1 MHz for the single and M-PNGs.

kHz to 1 MHz can be determined according to the following Eq. (3):

$$\varepsilon_r(\omega) = C(\omega) \cdot D/\varepsilon_0 \cdot A \tag{3}$$

where ϵ_r = the dielectric constant, C= the capacitance, D = the composite thickness (\sim 80 µm), A = the electrode area (3.5 cm x 3.5 cm), ω = the angular frequency, and ϵ_{0} = the free space's dielectric constant (8.85×10⁻¹² F/m).

Analysis of the values achieved for the dielectric constants of all the specimens in Fig. 8 shows that the ϵ_r of the four-layered PNG device was 8.6 times higher than that of the single-layered PNG.

The dielectric constant (ϵ) is inversely proportional to the piezo-electric voltage constant ($g=d/\epsilon$) and directly proportional to the piezo-electric coefficient ($d=g.\epsilon$) value. A high dielectric constant is important for energy storage in capacitors, but it can negatively affect the voltage generation capacity in sensors. This situation requires careful material selection and design to optimize performance for specific piezo-electric applications, balancing voltage output, charge output, and other material properties such as flexibility or fracture toughness.

3.4. Piezoelectric properties of the M-PNGs

When reviewing the studies in the literature on layer-by-layer stacking of electrospun mats, the absence of aluminum sheets between the layers has revealed energy losses in the output power of PNGs because of various factors, such as interfacial effects [61,62], high internal impedance [63], a polarization reduction effect [64,65], and uneven stress and electric field distributions [66].

In the case of PNG without an aluminum metal layer between the layers, the applied stress affects the highest level only the top piezo layer, while the lower piezo layers are exposed to less stress due to the attenuation of the applied stress as it passes through the dielectric medium. The stress concentration that occurs when aluminum metal is used

between layers ensures that the stress applied to the upper piezo layer is distributed equally across each layer of the stacked piezo-nanofiber mat. Consequently, the piezoelectric device incorporating an aluminum metal layer generates a higher Maxwell displacement field than the device without one. This displacement field, which is produced by the displacement current, is the main driving force behind the piezoelectric device's power generation when subjected to repetitive mechanical impact [67].

The concept of the four layered PNG with a parallel connection according to the fiber mats' dipole moment direction, and its electrical circuit equivalent exhibited in Fig. 9. As demonstrated in our previous study, the existence of PZT particles in composite nanofibers has a more pronounced effect on improving the degree of crystallinity (χ_c) and the β -phase content-%F(β) in the composite structure compared to the GNP [68]. This improvement primarily results from the interaction between the PZT/GNP surfaces and the $-CH_2/-CF_2$ groups of the PVDF chains (Figs. 9a and b). Furthermore, during electrospinning, the ferroelectric domains of the PZT ceramics become aligned under the influence of the electric field. This spontaneous polarization improved the piezoelectricity by preventing the accumulation and migration of space charges in the composite structure and by increasing the average local electric field at the interface between the PZT ceramics and the PVDF chains [69].

On the other hand, the GNP-interacted PVDF nanocomposites resulted in more electron flow within the PNG by enhancing space charge transmission owing to the high charge carrier mobility of the conductive GNP. In the interaction of the PVDF/GNP composite nanofibers, the H atoms of the -CH₂/-CF₂ dipoles in the PVDF chains tend to approach the GNP surface (Fig. 9(b)). This proximity is because of electrostatic interactions between low-electronegativity H atoms in the PVDF chains and sp²-hybridized C atoms with π orbitals in the GNP [54]. This interaction results in the —CF₂— bonds in the composite nanofibers projecting away from the GNP surface, which promotes the formation of the β -crystal phase [70]. This dipole alignment contributes to a higher

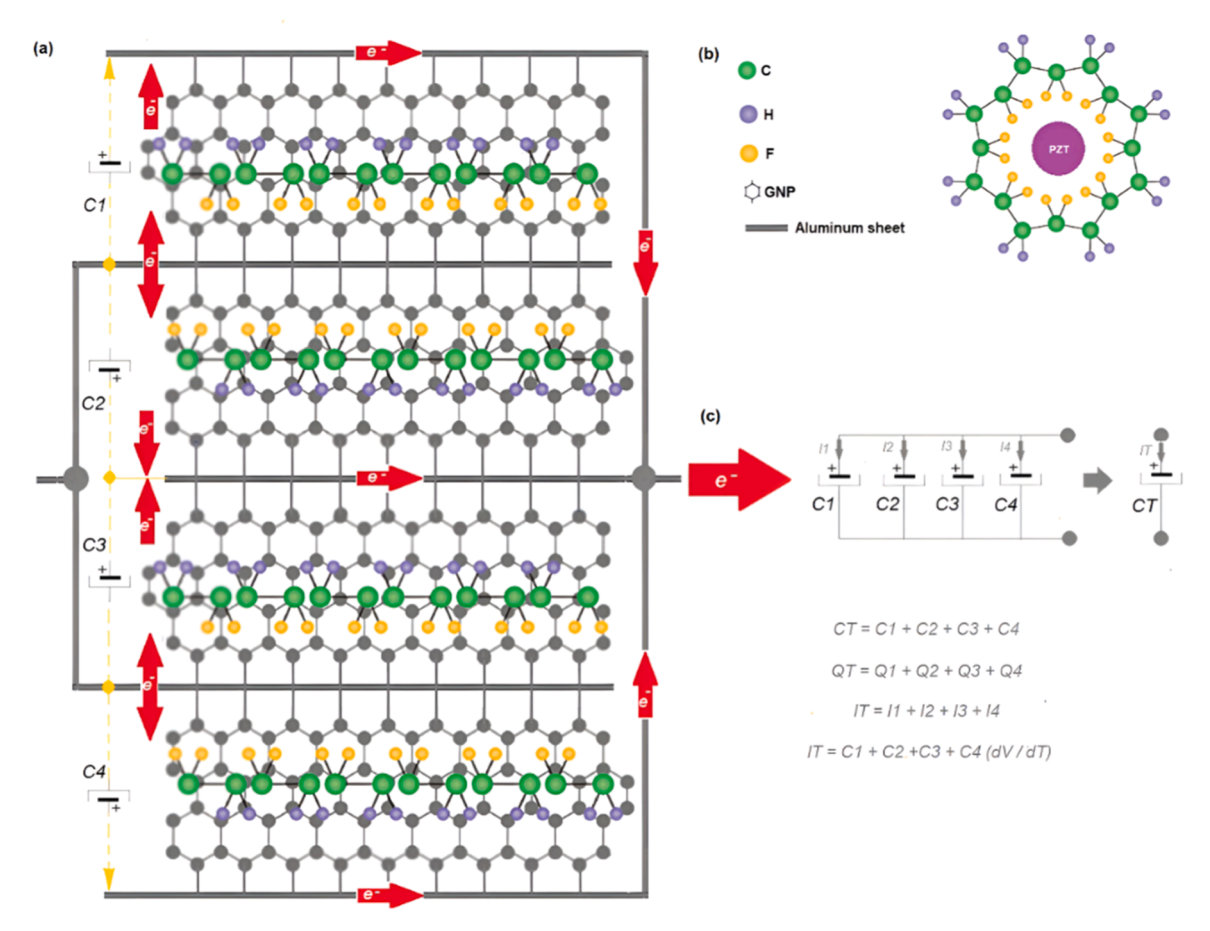


Fig. 9. The concept of the four-layered PNG with a parallel connection through aluminium sheets placed between the intermediate layer according to the fiber mats' dipole moment direction (a), the interaction between the PZT and the PVDF chains (b), and its electrical circuit equivalent (c).

net polarization of the crystal lattice, resulting in enhanced piezoelectric properties [71].

The four-layered PNG formed by the connection of the aluminium plates that are placed between the interlayers when producing the fiber mat (which becomes a polarized capacitor) according to the dipole moment direction results in four capacitors obtained that are connected in parallel in the same direction, as shown in Fig. 9c.

The capacitive model for both piezoelectric and triboelectric nanogenerators is referred to as capacitive conduction, where displacement current is the only conduction mechanism for transporting electricity. Power is transmitted through electromagnetic waves and induction rather than through the flow of free charges across the capacitor's electrodes [72]. According to the capacitor model, the output current of a PNG can be represented as follows:

$$I = \frac{dQ}{dt} = C\frac{dv}{dt} + V\frac{dC}{dt}$$
 (4)

where Q means the stored charges in the capacitor. In this equation, the first variable is the current introduced by a change in the applied voltage $(C\frac{dV}{dt})$, while the second variable is the current introduced by the variation in capacitance $(V\frac{dC}{dt})$. The second variable will become zero because each capacitor value is constant $(V\frac{dC}{dt}=0)[73]$

When the capacitors (PNGs) are connected in parallel, the equivalent capacitance (C_T : C_{Total}) in the circuit is equal to the sum of all PNGs. The charging current flowing through the individual PNGs (C_1 , C_2 , C_3 , and C_4) is related to the voltage across each of the PNG. Therefore, the charging currents of the PNGs are given by the following equations:

$$I_{T} = I_{1} + I_{2} + I_{3} + I_{4} \tag{5}$$

$$IT = C1\frac{dV1}{dt} + C2\frac{dV2}{dt} + C3\frac{dV3}{dt} + C4\frac{dV4}{dt}$$
 (6)

In a circuit with parallel-connected PNGs, the voltage value of each PNG is equal to the voltage value (V) applied to the circuit ($V=V_1=V_2=V_3=V_4$)

Finally, Eq. (7) can be written as,

$$IT = (C1 + C2 + C3 + C4) \frac{dV}{dt}$$
 (7)

Since the total capacity value of parallel connected PNGs will increase according to Kirchhoff's circuit laws, an increase in the total current (I_T) value to be drawn from the PNGs is also expected.

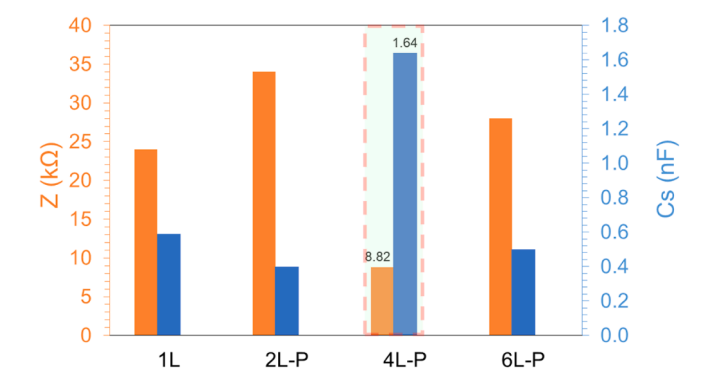


Fig. 10. The impedance and the capacitance alternate with single and M-PNGs at a frequency of $10\ kHz$.

Fig. 10 shows the experimental findings in which the four-layered PNG with the highest capacitance value were found to have 2.7 times more capacity compared to the single-layered PNG.

Taking into consideration the impedance (Z) changes of all the samples, an increase in their capacitance values results in a decrease in their impedance values according to Eq. (8).

$$Z = \frac{1}{2\pi fc} \tag{8}$$

where Z= the impedance, f= the measurement frequency, and C= the capacitance.

In order to determine the piezoelectric properties of the PNGs, the Thevenin, Norton and maximum power theorems expressed in two-terminal network systems were utilized. According to these theorems, the V_{OC} , I_{SC} and P_{MAX} values associated with the PNG can be defined as expressed in Eqs. (9) and (10) [73].

$$R_{TH} = \frac{V_{OC}}{I_{SC}} \tag{9}$$

$$P_{Max} = \frac{(V_{TH})^2}{4R_{TH}} = \frac{(V_{OC})^2}{4R_L}$$
 (10)

where the Thevenin voltage- V_{TH} is equal to the V_{OC} , while the Thevenin resistance- R_{TH} is equivalent to the load resistance- R_{L} .

Fig. 11 shows the PEHS that was employed to determine the piezo-electric performances of the single-layered and M-PNGs.

The PEHS occurs in a magnetic shaker, which is controlled by a frequency generator and a power amplifier, and it is connected to an aluminum cantilever beam that vibrates in response to this magnetic shaker.

In order to collect V_{OC} data obtained from the PNG, a data acquisition card (NI 6009) supported by NI LabViewTM software was employed, while their I_{SC} currents were measured through a low noise current amplifier (LMC-6001). According to scientific literature, peak-to-peak voltage (VPP) variations are taken into account in PNG performance

evaluations. However, given the non-sinusoidal nature of the PNG output voltages, V_{PP} may not be the most appropriate or robust form of measurement. Root Mean Square (RMS) voltage values should be considered as a potentially more appropriate and informative metric for comparisons, which can better represent the overall signal magnitude, especially for non-ideal waveforms. Therefore, the V_{OC} and I_{SC} values were calculated as V_{RMS} and I_{SC} (I_{RMS}) using the equations V_{RMS}

$$\sqrt{rac{1}{T^*}\int_0^T Voc(t)^2 dt}$$
 and $I_{RMS} = \sqrt{rac{1}{T^*}\int_0^T Isc(t)^2 dt}$, respectively.

The output voltage changes (open circuit voltage- V_{OC}) associated with PNGs are demonstrated as V_{PP} and V_{RMS} in Fig. 12.

At a resonance frequency of 20 Hz, the maximum V_{RMS} values of 182.69 mV for the four-layered PNG with a parallel connection were measured, while the output voltage value for the single-layered PNG is defined as 45.38 mV (V_{RMS}) at 10 Hz.

As seen in Fig. 13, when the samples' electrode tips were shorted, the I_{SC} changes of all samples were measured for the single and M-PNGs at 20 Hz, and the highest I_{RMS} value of 3.65 μA was reached for the four-layered PNG.

The V_{RMS} , I_{RMS} , and P_{RMS} changes of all samples are depicted in detail in Fig. 14.

The results of the experiment show that under a load of 50 K Ω , the highest P_{RMS} of 0.166 μW was reached by drawing a 1.82 μA current from the four-layered PNG. The electrical power of the four-layered PNG was approximately 4.38 times than that of the single-layered PNG at a resonance frequency of 20 Hz.

3.5. Design of a remote monitoring system based on the IoT

An IoT connectivity platform manages and monitors communication protocols that connect devices via Wi-Fi, Bluetooth, and the mobile internet, etc. These platforms provide a user-friendly interface for provisioning and managing devices across the networks as needed. The accurate and precise measurement, transfer, processing, and evaluation of the voltage or the current that is generated by the PNGs play a crucial

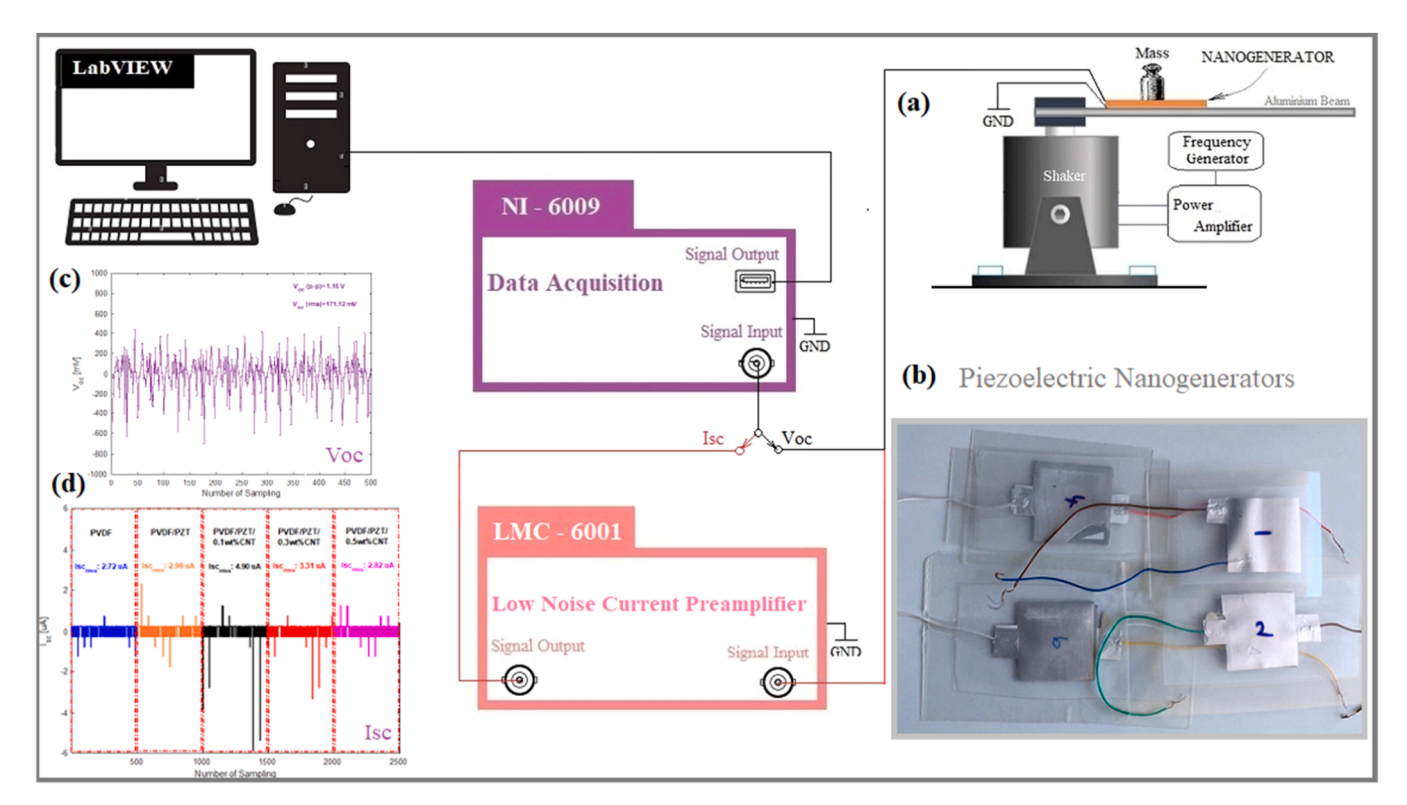


Fig. 11. The PEHS (a), PNGs' photographs (b), the symbolic V_{OC} (c), and the symbolic I_{SC} (d) graphs.

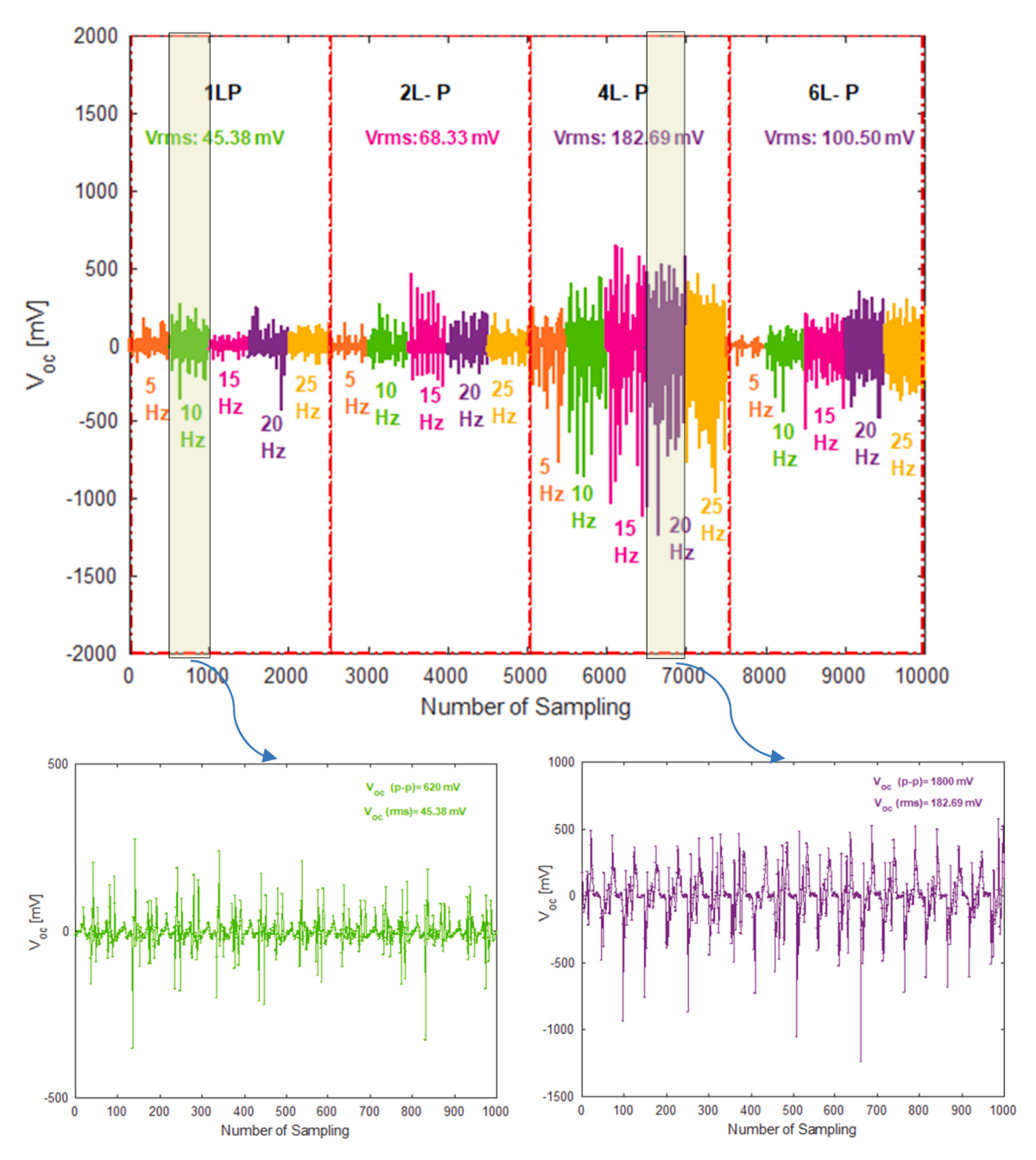


Fig. 12. The V_{OC} and V_{RMS} changes of the single and M-PNGs.

role in various scientific applications. Wireless transfer methods are often preferred for acquiring data from PNGs, enabling remote monitoring of information related to meteorology, structural health, and human health [74–76].

Although the high output impedance of the PNGs poses a critical challenge in designing measurement circuits, the input impedance of measurement circuits must also be high in order to minimize the impact of the output impedance. Fig. 15 indicates the circuit diagram of the remote voltage measurement system for the PNG.

In this design, the LM358B operational amplifier (op-amp) was chosen for the PNG remote voltage measurement system because of its advantageous features, such as high input impedance and the ability to operate with a single energy source. An op-amp-based voltage follower (OP1) was used to measure the PNG voltage in the system. The value of the load resistor (R_L) connected in parallel to the PNG was found to be equal to the PNG output impedance of 1 M Ω . In the remote measurement

system, the PNG voltage was sampled and converted into digital data by the microcontroller. To ensure compatibility with the microcontroller's Analog-to-Digital Converter (ADC) input voltage range of 0 to 3.3 Volts, a non-inverting voltage shifter circuit using an LM358B op-amp (OP2) was utilized. In this circuit, the PG and PS potentiometers were used in order to fine-tune the gain and voltage shift levels, respectively.

The microcontroller processes the analog signal at a frequency of 250 Hz at the ADC input. The internal ADC unit of the microcontroller converts the analogue voltage values obtained from the PNG into digital data according to Eq. (11).

$$A[n] = \frac{2^{12}}{\nu_{ref}} (x[n] + \nu_{bias}) \tag{11}$$

where v_{ref} is the reference voltage of the ADC unit, v_{bias} is the offset voltage that is provided by the voltage shifter circuit, x[n] is the PNG output voltage, and A[n] is the digital value produced by the ADC unit.

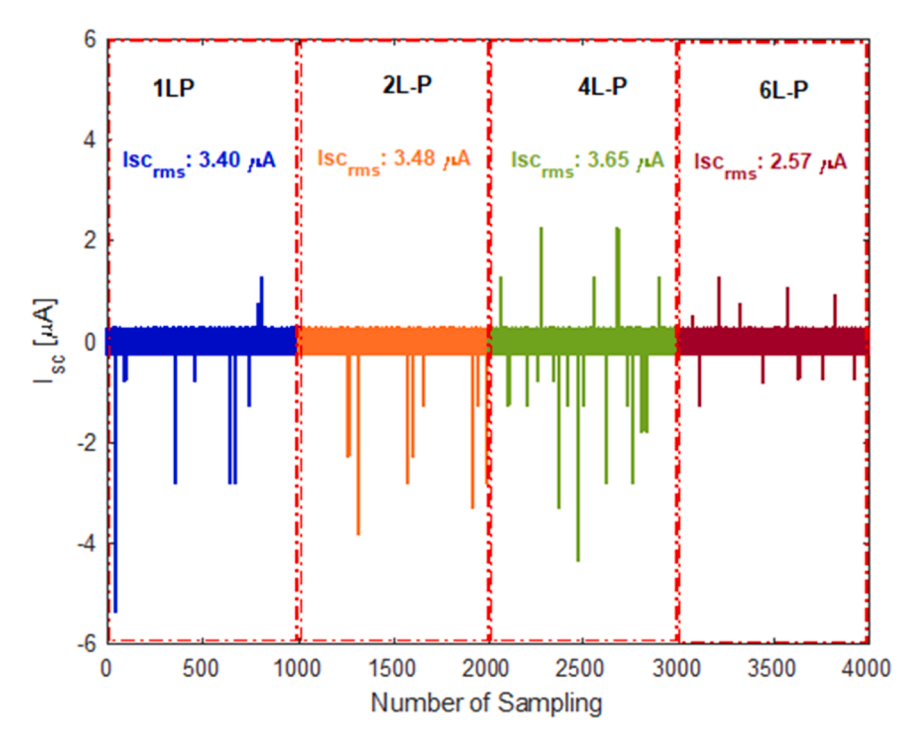


Fig. 13. The I_{SC} and I_{RMS} changes of the single and M-PNGs.

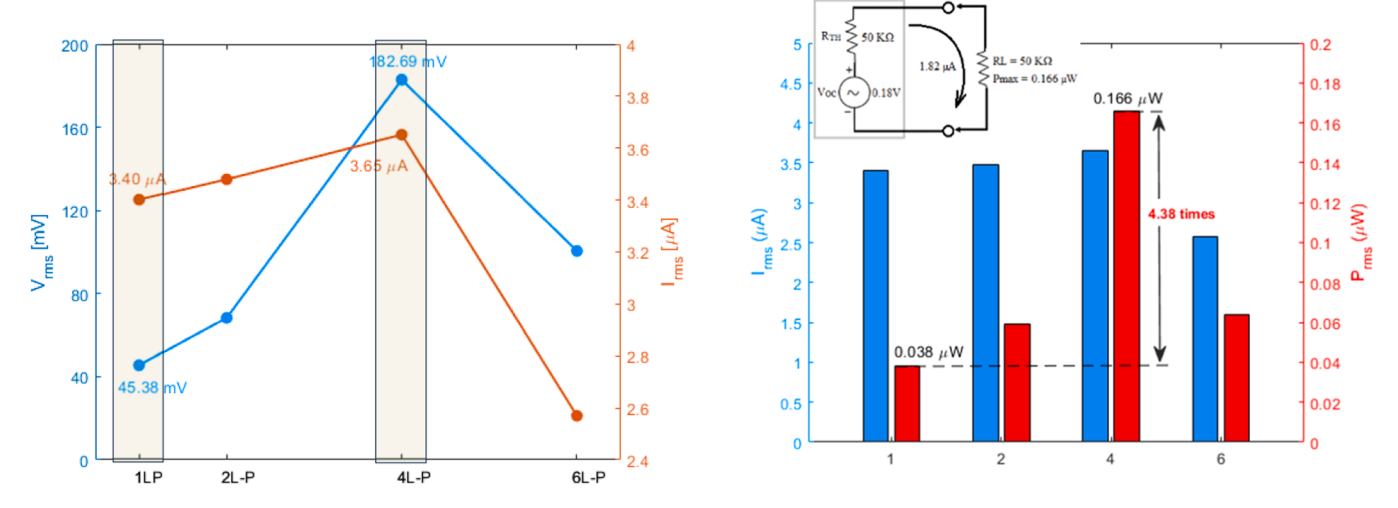


Fig. 14. Comparing the V_{RMS} , the I_{RMS} , and the $P_{MAX\text{-}RMS}$ values for single and M-PNGs.

This digital data is broadcast via a Bluetooth Communication board (HC-06) so that other connected devices can receive it. In the designed circuit, an ARM-based microcontroller (STM32F103C8T6 BluePill), equipped with internal ADC and Universal Asynchronous Receiver-Transmitter (UART) units, is employed to measure the PNG voltage signal and digitize it with a resolution of 12 bits. The digitized signal is then transmitted to the Bluetooth Communication card through the UART terminal, operating at an asynchronous baud rate of 115,200. The list of electronic materials used in the circuit is given in detail in Table 3.

Fig. 16 displays a photo of the electronic components mounted to the printed circuit board (PCB). The data transmitted by the remote measurement system using a Bluetooth protocol can be monitored via a computer or mobile device for recording and visualisation purposes. In order to monitor the system developed in this study on the computer screen, an interface programme was developed through the Visual Studio 2022 platform. The human machine interface (HMI) program, whose

screenshot is presented in Fig. 17(d), is designed to receive, store and display the PNG voltage data transmitted over the air via Bluetooth device in the desired format, which is then displayed as analysis graphs on the computer screen. Using this software, raw data obtained from the ADC output can be stored in a database. Real voltage values can be displayed by multiplying the raw data by adjustable gain coefficients. The software enables users to create graphs for various datasets in different colors and offers the flexibility to modify both the voltage and the time axes. Furthermore, the offset bias effect introduced by the voltage shifter circuit (ν_{bias}) can be effectively eliminated through an appropriate subtraction operation.

3.6. The capacitor charging for energy harvesting

It is not possible to directly power portable microwatt-level electronic devices by harvesting energy from environmental sources through

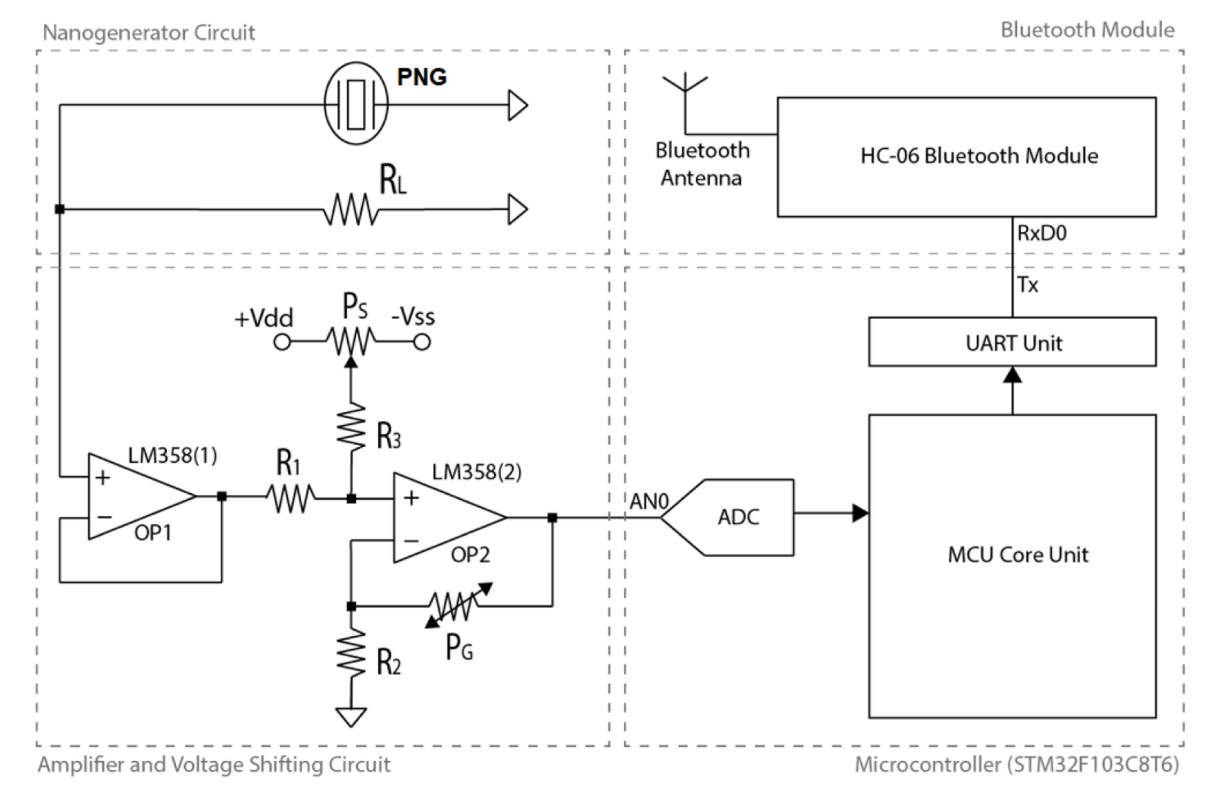


Fig. 15. Schematic diagram of the remote voltage monitoring system designed for the PNG.

Table 3 Electronic components list used in the remote voltage monitoring.

Component Value/Component ID
LM358B
STM32F103C8T6 BluePill
HC-06
1 ΜΩ
R2=1 k Ω , R1=2.2 k Ω , R3=20 k Ω
100 kΩ
20 kΩ

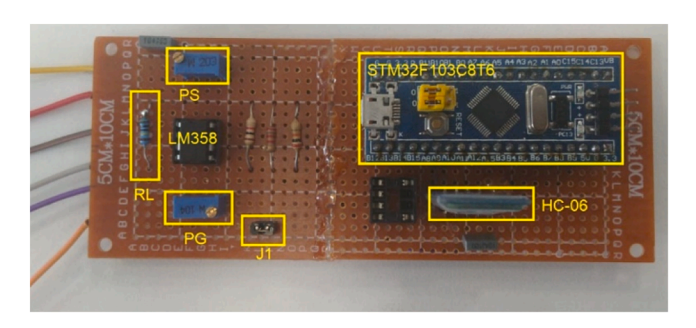


Fig. 16. Fabricated PCB board of the remote voltage monitoring system.

PNGs with nanowatt-level power capacity and high output impedance [77]. For that reason, the voltages obtained from the PNG device are matched to a low impedance load through an impedance matching circuit [78]. Fig. 17(a) depicts an energy harvesting system consisting of an impedance matching circuit, a full-wave rectifier (bridge diode), and a capacitor of 4.7 μ F.

According to $E=\frac{1}{2}CV^2$ (where E is the energy stored within a capacitor of 4.7 μF (C) and V is the voltage across the capacitor tips, or the potential difference between them), the electrical energy stored in the capacitor is calculated as 35.74 $\mu J.$

In this study, at a vibrational frequency of 20 Hz under an impact force of 1 N, the PVDF/PZT/1.5GNP-based four-layered PNG was fully charged up to 3.97 V after 30 s, which enhanced the charging voltage (2.2 V) to a rate of 80 % of the single-layered PNG.

As mentioned in Section 3.3, the four-layered PNG, which had a dielectric constant 8.6 times greater than that of the single-layered one, also caused to enhancement of the capacitor's charging output voltage by 1.8 times.

4. Conclusions

Multilayer fiber mats based on the PVDF/PZT/1.5GNP, which are constructed by placing an aluminum sheet between the layers, were successfully fabricated using a parallel connection design and a conventional pressing method. According to the Thevenin, Norton, and maximum power transfer theorems, the four-layered PNG has V_{OC} of 0.18 V (V_{RMS}) compared to a single-layered PNG, and it reached its highest power capacity of 166 nW when drawing a 1.82 µA current under a load of 50 K Ω . The four-layered PNG had a capacitance value that was 2.7 times higher than that of the single-layered PNG. This resulted in an electrical power efficiency ratio that was 380 % greater at a vibration frequency of 20 Hz and an impact force of 1 N. The presence of well-dispersed and adhered to conductive nanoparticle GNPs in the single-layered PVDF/PZT composite structure supports more electron flow due to the high charge carrier density, which occurs in the composite structure. In order to obtain MLS, aluminum sheets were placed between the stacked nanofiber mats (instead of stacking single-layered electrospun nanofibers without aluminum), and the mechanical vibration applied to the composite structure was distributed effectively in order to reach the other layers through the aluminum sheets in the intermediate layers. These results show that the piezoelectric performance of the parallel-connected M-PNG depends not only on the number of layers and the utilization of aluminum sheets that are placed between them, but also on the stacking arrangement concerning the dipole moment direction. The combination of two-dimensional graphene-

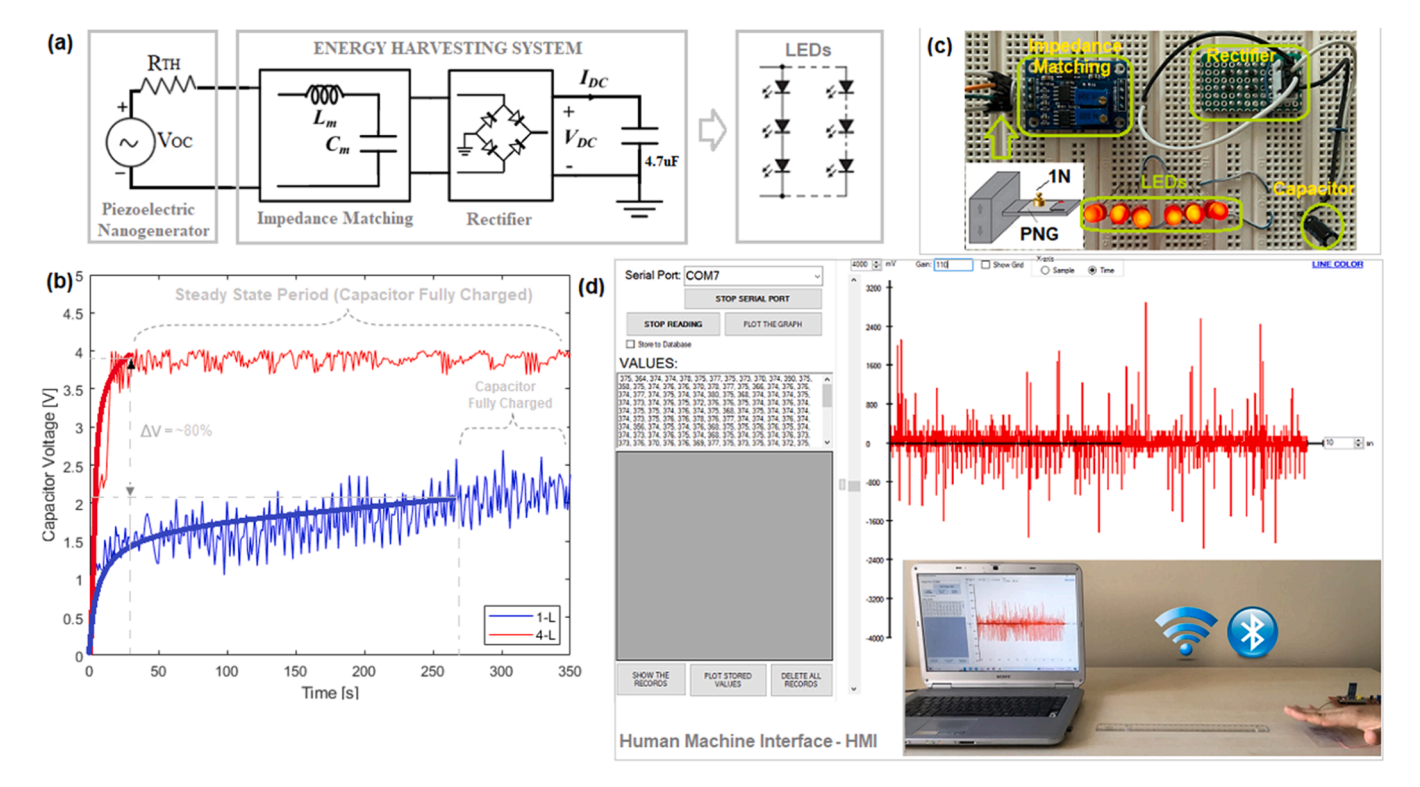


Fig. 17. The energy harvesting system employed for the capacitor charging (a), the charging as a time-dependent process of a commercial capacitor by single- and four-layered PNGs (b), six LEDs (Light Emitting Diodes) brightened via a capacitor of 4.7 μF and charged by a four-layered PNG (c), and an HMI screen (d).

containing electropun fiber mats with parallel connection techniques in order to obtain three-dimensional templates provides an excellent opportunity for advanced material applications. Furthermore, for the purpose of the highest power output from PNGs, future studies will focus on hybrid energy harvesting designs that allow energy to be harvested simultaneously from piezoelectric and triboelectric properties.

CRediT authorship contribution statement

Ertuğrul Karakulak: Methodology, Investigation, Formal analysis, Data curation. Levent Paralı: Writing – review & editing, Writing – original draft, Supervision, Methodology, Investigation, Formal analysis, Data curation, Conceptualization. Muhterem Koç: Methodology, Funding acquisition, Formal analysis, Data curation, Conceptualization. Farida Tatardar: Methodology, Investigation, Formal analysis. Ali Sarı: Visualization, Validation, Resources, Formal analysis, Data curation. Ersoy Mevsim: Visualization, Software, Resources, Data curation. Valida Fataliyeva: Visualization, Validation, Methodology, Investigation.

Declaration of competing interest

The authors declare that they have no known competing financial interests or personal relationships that could have appeared to influence the work reported in this paper.

Acknowledgment

The authors would like to thank the staff of Kutahya Dumlupınar University Advanced Technologies Research Center (DPU-ILTEM) for performing SEM, XRD, and FTIR analyses.

Data availability

Data will be made available on request.

References

- [1] X. Hu, L. Xu, X. Lin, M. Pecht, Battery lifetime prognostics, Joule 4 (2020) 310–346, https://doi.org/10.1016/j.joule.2019.11.018.
- [2] L. Lu, W. Ding, J. Liu, B. Yang, Flexible PVDF based piezoelectric nanogenerators, Nano Energy 78 (2020), https://doi.org/10.1016/j.nanoen.2020.105251.
- [3] N.P. K. A. Chandrasekhar, Marriage between metal-organic frameworks/covalent-organic frameworks and triboelectric nanogenerator for energy harvesting —A review, Mater. Today Energy 37 (2023), https://doi.org/10.1016/j.mtener.2023.101393.
- [4] R.L. Harne, K.W. Wang, A review of the recent research on vibration energy harvesting via bistable systems, Smart Mater. Struct. 22 (2013), https://doi.org/ 10.1088/0964-1726/22/2/023001.
- [5] S. Korkmaz, A. Kariper, Pyroelectric nanogenerators (PyNGs) in converting thermal energy into electrical energy: fundamentals and current status, Nano Energy 84 (2021), https://doi.org/10.1016/j.nanoen.2021.105888.
- [6] F. Rigo, M. Migliorini, A. Pozzebon, Piezoelectric sensors as energy harvesters for ultra low-power IoT applications, Sensors 24 (2024), https://doi.org/10.3390/ s24082587.
- [7] I. Rojek, D. Mikołajewski, A. Mroziński, M. Macko, T. Bednarek, K. Tyburek, Internet of things applications for energy management in buildings using artificial intelligence—A case study, Energies (2025) 18, https://doi.org/10.3390/ en18071706.
- [8] Y. Xie, Flexible nanogenerators for energy harvesting and self-powered biomedical devices, in: ECS Meeting Abstracts MA2019-01, 2019, p. 1347, https://doi.org/ 10.1149/ma2019-01/27/1347.
- [9] H. Luo, T. Yang, X. Jing, Y. Cui, W. Qin, Environmental energy harvesting boosts self-powered sensing, Mater. Today Energy 40 (2024), https://doi.org/10.1016/j. mteper 2024 101502
- [10] S. Al-Sarawi, M. Anbar, R. Abdullah, A.B.Al Hawari, Internet of things market analysis forecast, 2020-2030, 2020, in: Fourth World Conference on Smart Trends in Systems, Security and Sustainability (WorldS4), 2020, https://doi.org/10.1109/ WorldS450073.2020.9210375.
- [11] F.N. Tatardar, M.A. Kurbanov, I.S. Ramazanova, G.K. Guliyeva, A. Nuraliyev, Z. A. Dadashov, New materials for the electromechanical and acoustoelectric transducers, Ferroelectrics 606 (2023) 30–38, https://doi.org/10.1080/00150193.2023.2189840.
- [12] M. Aradoaei, A.M. Lucaci, R.C. Ciobanu, C. Schreiner, B.G. Rusu, G.E. Hitruc, M. Aflori, M. Paulet, A.R. Caramitu, A.M. Bors, Piezoelectric thin film composites with BaTiO3 for microelectronics, Mater. Plast. 60 (2023) 10–30, https://doi.org/ 10.37358/MP.23.4.5683.
- [13] M. Rahman, J. Haider, T. Akter, M.S.J. Hashmi, Techniques for assessing the properties of advanced ceramic materials, Compr. Mater. Process. 1 (2014) 3–34, https://doi.org/10.1016/B978-0-08-096532-1.00124-2.

- [14] M.T. Sebastian, H. Jantunen, Polymer-ceramic composites of 0-3 connectivity for circuits in electronics: a review, Int. J. Appl. Ceram. Technol. 7 (2010) 415–434, https://doi.org/10.1111/j.1744-7402.2009.02482.x.
- [15] J.X. Zhang, J.Y. Dai, L.C. So, C.L. Sun, C.Y. Lo, S.W. Or, H.L.W. Chan, The effect of magnetic nanoparticles on the morphology, ferroelectric, and magnetoelectric behaviors of CFO/P(VDF-TrFE) 0-3 nanocomposites, J. Appl. Phys. 105 (2009), https://doi.org/10.1063/1.3078111.
- [16] Z. Yin, B. Tian, Q. Zhu, C. Duan, Characterization and application of PVDF and its copolymer films prepared by spin-coating and langmuir-blodgett method, Polymers (2019) 11, https://doi.org/10.3390/polym11122033.
- [17] J. Li, J. Deng, S. Zhang, W. Chen, J. Zhao, Y. Liu, Developments and challenges of miniature piezoelectric robots: a review, Adv. Sci. 10 (2023), https://doi.org/ 10.1002/advs.2023.05128
- [18] J. Liu, H. Tan, X. Zhou, W. Ma, C. Wang, N.M.A. Tran, W. Lu, F. Chen, J. Wang, H. Zhang, Piezoelectric thin films and their applications in MEMS: a review, J. Appl. Phys. 137 (2025), https://doi.org/10.1063/5.0244749.
- [19] Y. Jiang, M.H. Zhang, C.F. Wu, Z. Xu, Z. Li, J.T. Lu, H.F. Huang, J.J. Zhou, Y.X. Liu, T. Zhou, W. Gong, K. Wang, Low-field-driven large strain in lead zirconate titanium-based piezoceramics incorporating relaxor lead magnesium niobate for actuation, Nat. Commun. 15 (2024), https://doi.org/10.1038/s41467-024-53007-
- [20] D.A. Van Den Ende, B.F. Bory, W.A. Groen, S. Van Der Zwaag, Improving the d33 and g33 properties of 0-3 piezoelectric composites by dielectrophoresis, J. Appl. Phys. 107 (2010), https://doi.org/10.1063/1.3291131.
- [21] I. Babu, G. de With, Highly flexible piezoelectric 0-3 PZT-PDMS composites with high filler content, Compos. Sci. Technol. 91 (2014) 91–97, https://doi.org/ 10.1016/j.compscitech.2013.11.027
- [22] R. Sridhar, V. Amith, S. Aditya, A. Gangadhar, K.A. Vishnumurthy, Electrospun PVDF/Cloisite-30B and PVDF/BaTio3/graphene nanofiber mats for development of nanogenerators, J. Indian Chem. Soc. 99 (2022), https://doi.org/10.1016/j. jics.2022.100501.
- [23] S.K. Ghosh, A. Biswas, S. Sen, C. Das, K. Henkel, D. Schmeisser, D. Mandal, Yb3+ assisted self-polarized PVDF based ferroelectretic nanogenerator: a facile strategy of highly efficient mechanical energy harvester fabrication, Nano Energy 30 (2016) 621–629, https://doi.org/10.1016/j.nanoen.2016.10.042.
- [24] X. Lin, F. Yu, X. Zhang, W. Li, Y. Zhao, X. Fei, Q. Li, C. Yang, S. Huang, Wearable piezoelectric films based on MWCNT-BaTiO3/PVDF composites for energy harvesting, sensing, and localization, ACS Appl. Nano Mater. 6 (2023) 11955–11965, https://doi.org/10.1021/acsanm.3c01792.
- [25] L. Meng, C. Yang, J. Meng, Y. Wang, Y. Ge, Z. Shao, G. Zhang, A.L. Rogach, H. Zhong, In-situ fabricated anisotropic halide perovskite nanocrystals in polyvinylalcohol nanofibers: shape tuning and polarized emission, Nano Res. 12 (2019) 1411–1416. https://doi.org/10.1007/s12274-019-2353-4.
- [26] J. Yang, Y. Zhang, Y. Li, Z. Wang, W. Wang, Q. An, W. Tong, Piezoelectric nanogenerators based on graphene oxide/PVDF electrospun nanofiber with enhanced performances by in-situ reduction, Mater. Today Commun. 26 (2021), https://doi.org/10.1016/j.mtcomm.2020.101629.
- [27] P. Viswanath, K.K.H. De Silva, H.H. Huang, M. Yoshimura, Large piezoresponse in ultrathin organic ferroelectric nano lamellae through self-assembly processing, Appl. Surf. Sci. 532 (2020), https://doi.org/10.1016/j.apsusc.2020.147188.
- [28] M.M. Abolhasani, K. Shirvanimoghaddam, M. Naebe, PVDF/graphene composite nanofibers with enhanced piezoelectric performance for development of robust nanogenerators, Compos. Sci. Technol. 138 (2017) 49–56, https://doi.org/ 10.1016/j.compscitech.2016.11.017.
- [29] S. Labihi, N. Chakhchaoui, A. Eddiai, M. El Achaby, M. Meddad, O. Cherkaoui, M. Mazroui, Enhancement of piezoelectric β-polymorph formation and properties of graphene oxide and PZT-incorporated in PVDF-HFP matrix for energy harvesting applications, Polym. Compos. 44 (2023) 2296–2304, https://doi.org/10.1002/ps.27245
- [30] N.D. Kulkarni, P. Kumari, Role of rGO on mechanical, thermal, and piezoelectric behaviour of PVDF-BTO nanocomposites for energy harvesting applications, J. Polym. Res. 30 (2023), https://doi.org/10.1007/s10965-023-03449-4.
- [31] B. Sankar, P. Ramadoss, Review on fiber hybridization in ternary blended highperformance concrete, in: Mater Today Proc, Elsevier Ltd, 2021, pp. 4919–4924, https://doi.org/10.1016/j.matpr.2021.01.366.
- [32] F.E. Hanana, D. Rodrigue, Effect of particle size, fiber content, and surface treatment on the mechanical properties of maple-reinforced LLDPE produced by rotational molding, Polym. Polym. Compos. 29 (2021) 343–353, https://doi.org/ 10.1177/0967391120916602.
- [33] M. Rajeev, C.C. Helms, A study of the relationship between polymer solution entanglement and electrospun PCL fiber mechanics, Polymers (2023) 15, https:// doi.org/10.3390/polym15234555.
- [34] M. Ahmadi Bonakdar, D. Rodrigue, Electrospinning: processes, structures, and materials, Macromol 4 (2024) 58–103, https://doi.org/10.3390/ macromol/4010004.
- [35] A.M. Al-Dhahebi, S.C.B. Gopinath, M.S.M. Saheed, Graphene impregnated electrospun nanofiber sensing materials: a comprehensive overview on bridging laboratory set-up to industry, Nano Converg. 7 (2020), https://doi.org/10.1186/ s40580-020-0237-4
- [36] X. Du, Z. Zhou, Z. Zhang, L. Yao, Q. Zhang, H. Yang, Porous, multi-layered piezoelectric composites based on highly oriented PZT/PVDF electrospinning fibers for high-performance piezoelectric nanogenerators, J. Adv. Ceram. 11 (2022) 331–344, https://doi.org/10.1007/s40145-021-0537-3.
- [37] Y. Li, J. Tan, K. Liang, Y. Li, J. Sun, H. Zhang, C. Luo, P. Li, J. Xu, H. Jiang, K. Wang, Enhanced piezoelectric performance of multi-layered flexible polyvinylidene fluoride–BaTiO3–rGO films for monitoring human body motions,

- J. Mater. Sci. Mate. Electron. 33 (2022) 4291–4304, https://doi.org/10.1007/s10854-021-07622-7.
- [38] Y. Zhang, M. Xie, J. Roscow, Y. Bao, K. Zhou, D. Zhang, C.R. Bowen, Enhanced pyroelectric and piezoelectric properties of PZT with aligned porosity for energy harvesting applications, J. Mater. Chem. A Mater. 5 (2017) 6569–6580, https://doi.org/10.1039/c7ta00967d.
- [39] B. Ameduri, A. Bruno, Copolymers: recent developments and future trends, Chem. Rev. 109 (2009) 6632–6686, https://doi.org/10.1021/cr800187mï.
- [40] P. Martins, A.C. Lopes, S. Lanceros-Mendez, Electroactive phases of poly (vinylidene fluoride): determination, processing and applications, Prog. Polym. Sci. 39 (2014) 683–706, https://doi.org/10.1016/j.progpolymsci.2013.07.006.
- [41] T. Lei, X. Cai, X. Wang, L. Yu, X. Hu, G. Zheng, W. Lv, L. Wang, D. Wu, D. Sun, L. Lin, Spectroscopic evidence for a high fraction of ferroelectric phase induced in electrospun polyvinylidene fluoride fibers, RSC Adv. 3 (2013) 24952–24958, https://doi.org/10.1039/c3ra42622i.
- [42] D.Y. Lee, J.Y. Park, K.H. Lee, J.H. Kang, Y.J. Oh, N.I. Cho, Synthesis and characterization of Pb(Zr0.5Ti0.5) O3 nanofibers, Curr. Appl. Phys. 11 (2011) 1139–1143, https://doi.org/10.1016/j.cap.2011.02.011.
- [43] L. Shi, H. Jin, S. Dong, S. Huang, H. Kuang, H. Xu, J. Chen, W. Xuan, S. Zhang, S. Li, X. Wang, J. Luo, High-performance triboelectric nanogenerator based on electrospun PVDF-graphene nanosheet composite nanofibers for energy harvesting, Nano Energy 80 (2021), https://doi.org/10.1016/j.nanoen.2020.105599.
- [44] C.H. Du, B.K. Zhu, Y.Y. Xu, Effects of stretching on crystalline phase structure and morphology of hard elastic PVDF fibers, J. Appl. Polym. Sci. 104 (2007) 2254–2259, https://doi.org/10.1002/app.25635.
- [45] J. Zhao, T. Li, H. Sun, Z. Lu, T. Xiong, D. Li, D. Sun, Regulated crystallization and piezoelectric properties of bio-based poly(L-lactic acid)/diatomite composite fibers by electrospinning, Adv. Compos. Hybrid Mater. 7 (2024), https://doi.org/ 10.1007/s42114-024-01034-x.
- [46] H.S. Jang, H.J. Park, G.H. Kim, C.M. Kim, N.R. Alluri, B.N. Bae, H.M. Jeon, D. H. Lee, K.Il Park, Dual-controlled piezoelectric composite film with enhanced crystallinity and defect-free via solvent vapor treatment, Nano Energy 136 (2025), https://doi.org/10.1016/j.nanoen.2025.110705.
- [47] R. Gregorio, M. Cestari, Effect of crystallization temperature on the crystalline phase content and morphology of poly(vinylidene fluoride), J. Polym. Sci. B Polym. Phys. 32 (1994) 859–870, https://doi.org/10.1002/polb.1994.090320509.
- [48] X. Cai, T. Lei, D. Sun, L. Lin, A critical analysis of the α, β and γ phases in poly (vinylidene fluoride) using FTIR, RSC Adv. 7 (2017) 15382–15389, https://doi. org/10.1039/c7ra01267e.
- [49] P. Lei, X. Xu, C. Huang, D. Chen, Z. Jiang, Promoting proton conductivity and methanol-resistance of PVdF-based PEM membrane by incorporating dispersive CNT dotted with α-Zr(HPO4)2•H2O, J. Appl. Polym. Sci. 142 (2025), https://doi. org/10.1002/app.57083.
- [50] L. Li, M. Zhang, M. Rong, W. Ruan, Studies on the transformation process of PVDF from α to β phase by stretching, RSC Adv. 4 (2014) 3938–3943, https://doi.org/ 10.1039/c3ra45134h.
- [51] Y. Peng, P. Wu, A two dimensional infrared correlation spectroscopic study on the structure changes of PVDF during the melting process, Polymer 45 (2004) 5295–5299, https://doi.org/10.1016/j.j.polymer.2004.05.034
- 5295–5299, https://doi.org/10.1016/j.polymer.2004.05.034.
 S. Janakiraman, A. Surendran, S. Ghosh, S. Anandhan, A. Venimadhav, Electroactive poly(vinylidene fluoride) fluoride separator for sodium ion battery with high coulombic efficiency, Solid State Ion. 292 (2016) 130–135, https://doi. org/10.1016/j.ssi.2016.05.020.
- [53] N. Chakhchaoui, R. Farhan, A. Eddiai, M. Meddad, O. Cherkaoui, M. Mazroui, Y. Boughaleb, L. van Langenhove, Improvement of the electroactive b-phase nucleation and piezoelectric properties of PVDF-HFP thin films influenced by TiO2 nanoparticles, in: Mater Today Proc, Elsevier Ltd, 2019, pp. 1148–1152, https:// doi.org/10.1016/i.matpr.2020.05.407.
- [54] C.L. Liang, Z.H. Mai, Q. Xie, R.Y. Bao, W. Yang, B.H. Xie, M.B. Yang, Induced formation of dominating polar phases of poly(vinylidene fluoride): positive ion-CF2 dipole or negative ion-CH2 dipole interaction, J. Phys. Chem. B 118 (2014) 9104–9111, https://doi.org/10.1021/jp504938f.
- [55] W. Zhou, X. Jiang, P. Wang, H. Wang, Geometric constraint annealing leading to β-phase enhancement of electrospun poly(vinylidene fluoride), Fibers Polym. 14 (2013) 100-104. https://doi.org/10.1007/s12221-013-0100-0
- (2013) 100–104, https://doi.org/10.1007/s12221-013-0100-0.
 [56] H. Dong, K. Xiao, X. Tang, Z. Zhang, J. Dai, R. Long, W. Liao, Preparation and characterization of polyurethane (PU)/polyvinylidene fluoride (PVDF) blending membrane, Desalin. Water Treat 57 (2016) 3405–3413, https://doi.org/10.1080/19443994.2014.988659.
- [57] M. Sang, S. Wang, M. Liu, L. Bai, W. Jiang, S. Xuan, X. Gong, Fabrication of a piezoelectric polyvinylidene fluoride/carbonyl iron (PVDF/CI) magnetic composite film towards the magnetic field and deformation bi-sensor, Compos. Sci. Technol. 165 (2018) 31–38, https://doi.org/10.1016/j.compscitech.2018.06.006.
- [58] J.Y. Lim, S. Kim, Y. Seo, Enhancement of β-phase in PVDF by electrospinning, in: AIP Conf Proc, American Institute of Physics Inc., 2015, https://doi.org/10.1063/ 1.101441.
- [59] C.M. Wu, M.H. Chou, Polymorphism, piezoelectricity and sound absorption of electrospun PVDF membranes with and without carbon nanotubes, Compos. Sci. Technol. 127 (2016) 127–133, https://doi.org/10.1016/j. compscitech.2016.03.001.
- [60] S. Mirjalali, R. Bagherzadeh, S. Abrishami, M. Asadnia, S. Huang, A. Michael, S. Peng, C.H. Wang, S. Wu, Multilayered electrospun/electrosprayed polyvinylidene fluoride+zinc oxide nanofiber mats with enhanced piezoelectricity, Macromol. Mater. Eng. 308 (2023), https://doi.org/10.1002/mame.202300009.

- [61] C.R. Bowen, H.A. Kim, P.M. Weaver, S. Dunn, Piezoelectric and ferroelectric materials and structures for energy harvesting applications, Energy Environ. Sci. 7 (2014) 25–44, https://doi.org/10.1039/c3ee42454e.
- [62] H. Luo, X. Zhou, C. Ellingford, Y. Zhang, S. Chen, K. Zhou, D. Zhang, C.R. Bowen, C. Wan, Interface design for high energy density polymer nanocomposites, Chem. Soc. Rev. 48 (2019) 4424–4465, https://doi.org/10.1039/c9cs00043g.
- [63] B. Sun, X. Li, R. Zhao, H. Ji, J. Qiu, N. Zhang, D. He, C. Wang, Electrospun poly (vinylidene fluoride)-zinc oxide hierarchical composite fiber membrane as piezoelectric acoustoelectric nanogenerator, J. Mater. Sci. 54 (2019) 2754–2762, https://doi.org/10.1007/s10853-018-2985-x.
- [64] S.K. Ghosh, D. Mandal, Synergistically enhanced piezoelectric output in highly aligned 1D polymer nanofibers integrated all-fiber nanogenerator for wearable nano-tactile sensor, Nano Energy 53 (2018) 245–257, https://doi.org/10.1016/j. nanoen.2018.08.036.
- [65] J. Park, M. Kim, Y. Lee, H.S. Lee, H. Ko, Nanomaterials: fingertip skin-inspired microstructured ferroelectric skins discriminate static/dynamic pressure and temperature stimuli, Sci. Adv. (2015) 1, https://doi.org/10.1126/sciadv.1500661.
- [66] W. Zeng, X.M. Tao, S. Chen, S. Shang, H.L.W. Chan, S.H. Choy, Highly durable all-fiber nanogenerator for mechanical energy harvesting, Energy Environ. Sci. 6 (2013) 2631–2638, https://doi.org/10.1039/c3ee41063c.
- [67] B. Mahanty, S.K. Ghosh, G. Prasad, A. Shanmugasundaram, D.W. Lee, Giant energy harvesting via Maxwell displacement current enhancement using metal sheet interspaced hetero-layer structured piezo-composite nanofiber device, Adv. Funct. Mater. 34 (2024), https://doi.org/10.1002/adfm.202307723.
- [68] L. Paralı, F. Tatardar, M. Koç, A. Sarı, R. Moradi, The piezoelectric response of electrospun PVDF/PZT incorporated with pristine graphene nanoplatelets for mechanical energy harvesting, J. Mater. Sci. Mate. Electron. 35 (2024), https:// doi.org/10.1007/s10854-023-11798-5.

- [69] S.K. Ghosh, J. Kim, M.P. Kim, S. Na, J. Cho, J.J. Kim, H. Ko, Ferroelectricity-coupled 2D-MXene-based hierarchically designed high-performance stretchable triboelectric nanogenerator, ACS Nano 16 (2022) 11415–11427, https://doi.org/10.1021/acsnano.2c05531.
- [70] R.P.S. Chakradhar, G. Prasad, P. Bera, C. Anandan, Stable superhydrophobic coatings using PVDF-MWCNT nanocomposite, in: Appl Surf Sci, Elsevier B.V., 2014, pp. 208–215, https://doi.org/10.1016/j.apsusc.2014.02.044.
- [71] B. Ameduri, From vinylidene fluoride (VDF) to the applications of VDF-ContainingPolymers and copolymers: recent developments and future trends, Chem. Rev. 109 (2009) 6632–6686, https://doi.org/10.1021/cr800187m.
- [72] Z.L. Wang, On Maxwell's displacement current for energy and sensors: the origin of nanogenerators, Mater. Today 20 (2017) 74–82, https://doi.org/10.1016/j. mattod.2016.12.001.
- [73] M.A. Salam, O.M. Rahman, in: Fundamentals of Electrical Circuit Analysis, 2018.
- [74] K. ichiro Kitamura, R. Takeuchi, K. Ogai, Z. Xin, W. Chen, T. Nemoto, Development of a novel pulse wave velocity measurement system: using dual piezoelectric elements, Med. Eng. Phys. 36 (2014) 927–932, https://doi.org/10.1016/j. medengphy.2014.02.024.
- [75] B. Mahanty, S. Mondal, U. Sahu, S. Patra, D. Mandal, Human health monitoring system based on piezoelectric smart sensor, in: International Conference on Computer, Electrical & Communication Engineering (ICCECE), 2016, pp. 1–4.
- [76] D. Rodenas-Herraíz, X. Xu, P.R.A. Fidler, K. Soga, Power-efficient piezoelectric fatigue measurement using long-range wireless sensor networks, Smart Mater. Struct. (2019) 28, https://doi.org/10.1088/1361-665X/ab2c46.
- [77] M. Safaei, H.A. Sodano, S.R. Anton, A review of energy harvesting using piezoelectric materials: State-of-the-art a decade later (2008-2018), Smart Mater. Struct. (2019) 28, https://doi.org/10.1088/1361-665X/ab36e4.
- [78] C.W. de Silva, Sensors For Control in Encyclopedia of Physical Science and Technology, 3rd ed., Academic Press, San Diago, 2003, p. 609.